Inorganic Chemistry

Article

pubs.acs.org/IC

Nanoindentation, High-Temperature Behavior, and Crystallographic/Spectroscopic Characterization of the High-Refractive-Index Materials $TiTa_2O_7$ and $TiNb_2O_7$

Lukas Perfler,*,[†] Volker Kahlenberg,[†] Christoph Wikete,[‡] Daniela Schmidmair,[†] Martina Tribus,[†] and Reinhard Kaindl[§]

[†]Institute of Mineralogy and Petrography, University of Innsbruck, Innrain 52f, 6020 Innsbruck, Austria

[‡]Institute for Structural Engineering and Material Sciences, Material Technology Innsbruck, University of Innsbruck, Technikerstr. 11/19a, 6020 Innsbruck, Austria

[§]Materials—Institute for Surface Technologies and Photonics, Functional Surfaces, JOANNEUM RESEARCH Forschungsgesellschaft mbH, Leobner Straße 94, 8712 Niklasdorf, Austria

Supporting Information

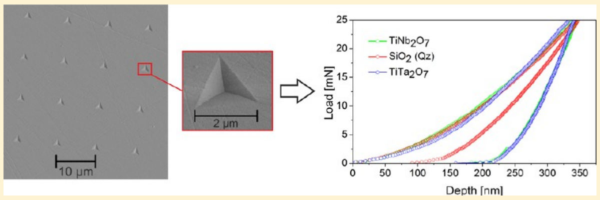

ABSTRACT: Colorless single crystals, as well as polycrystalline samples of $TiTa_2O_7$ and $TiNb_2O_7$, were grown directly from the melt and prepared by solid-state reactions, respectively, at various temperatures between 1598 K and 1983 K. The chemical composition of the crystals was confirmed by wavelength-dispersive X-ray spectroscopy, and the crystal structures were determined using single-crystal X-ray diffraction. Structural investigations of the isostructural compounds resulted in the following basic crystallographic data: monoclinic symmetry, space group $I2/m$ (No. 12), a = 17.6624(12) Å, b = 3.8012(3) Å, c = 11.8290(9) Å, β = 95.135(7)°, V = 790.99(10) Å^3 for $TiTa_2O_7$ and a = 17.6719(13) Å, b = 3.8006(2) Å, c = 11.8924(9) Å, β = 95.295(7)°, V = 795.33(10) Å^3, respectively, for $TiNb_2O_7$, Z = 6. Rietveld refinement analyses of the powder X-ray diffraction patterns and Raman spectroscopy were carried out to complement the structural investigations. In addition, *in situ* high-temperature powder X-ray diffraction experiments over the temperature range of 323−1323 K enabled the study of the thermal expansion tensors of $TiTa_2O_7$ and $TiNb_2O_7$. To determine the hardness (H), and elastic moduli (E) of the chemical compounds, nanoindentation experiments have been performed with a Berkovich diamond indenter tip. Analyses of the load−displacement curves resulted in a hardness of $H = 9.0 \pm 0.5$ GPa and a reduced elastic modulus of $E_r = 170 \pm 7$ GPa for $TiTa_2O_7$. $TiNb_2O_7$ showed a slightly lower hardness of $H = 8.7 \pm 0.3$ GPa and a reduced elastic modulus of $E_r = 159 \pm 4$ GPa. Spectroscopic ellipsometry of the polished specimens was employed for the determination of the optical constants n and k. $TiNb_2O_7$ as well as $TiTa_2O_7$ exhibit a very high average refractive index of $n_D = 2.37$ and $n_D = 2.29$, respectively, at $\lambda = 589$ nm, similar to that of diamond ($n_D = 2.42$).

1. INTRODUCTION

So far, only a very limited number of colorless oxide compounds are known to exhibit both a refractive index comparable to diamond ($n_D = 2.42$) and a high Vickers hardness value ($H_V > 7.5$ GPa). One example fulfilling these premises is $SrTiO_3$ with a refractive index of $n_D = 2.41$[1] and a hardness between $H_V = 7.8$ GPa (ref 2) and 9.5 GPa (ref 3).

The existence of $TiNb_2O_7$ and $TiTa_2O_7$ was first reported by Roth and Coughanour[4] and Waring and Roth,[5] respectively, while studying the phase equilibrium relations in the systems $TiO_2-Nb_2O_5$ and $TiO_2-Ta_2O_5$. Waring and Roth additionally observed a congruent melting of $TiTa_2O_7$ at ∼1935 K. $TiNb_2O_7$ also melts congruently at ∼1771 K.[6] The monoclinic structure of $TiNb_2O_7$ single crystals was first described by Wadsley[7] in 1961, but the determination of the cation distribution among the five octahedrally coordinated different metal sites was not fully studied. Wadsley assumed a random distribution of niobium and titanium atoms in the metal positions (66.67% Nb, 33.33% Ti). In contrast to Wadsley,[7] Von Dreele and Cheetham[8] observed a substantial ordering of the cations among the metal sites by Rietveld analyses of powder neutron diffraction data with site occupancy values for titanium varying from 14.0% to 64.5% for $TiNb_2O_7$. The structure refinement of Von Dreele and Cheetham resulted in the following crystallographic data: space group $A2/m$, a = 11.890(5) Å, b = 3.804(2) Å, c = 20.373(9) Å, β = 120.199(3)°, Z = 6, with the profile residuals of R_p = 9.47% and R_{wp} = 9.03%. Gasperin[9] also studied the crystal structure of $TiNb_2O_7$ by single-crystal X-ray diffraction and confirmed a preferential occupation of one type of site by Ti atoms but reported in the crystallographic information file (CIF) that all five metal sites are occupied by 66.7% Nb atoms and 33.3% Ti atoms. The structure has been refined by Gasperin to a final residual of R = 0.065 for 915 reflections ($I \geq 3\sigma I$) with the lattice parameter a = 20.351(3) Å, b = 3.801(2) Å, c = 11.882(2) Å, β =

Received: April 3, 2015
Published: July 1, 2015

DOI: 10.1021/acs.inorgchem.5b00733
Inorg. Chem. 2015, 54, 6836−6848

Table 1. Crystal Data and Structure Refinement of $TiTa_2O_7$ and $TiNb_2O_7$

empirical formula	$TiTa_2O_7$	$TiNb_2O_7$
molar mass	521.67 g mol^{-1}	345.68 g mol^{-1}
temperature	293(2) K	293(2) K
crystal system	monoclinic	monoclinic
space group	$I12/m1$ (No. 12)	$I12/m1$ (No. 12)
unit-cell dimensions		
a	17.6624(12) Å	17.6719(13) Å
b	3.8012(3) Å	3.8006(2) Å
c	11.8290(9) Å	11.8924(9) Å
α	90°	90°
β	95.135(7)°	95.295(7)°
γ	90°	90°
volume	790.99(10) Å^3	795.33(10) Å^3
Z	6	6
density (calculated)	6.537 g cm^{-3}	4.314 g cm^{-3}
crystal size (mm)	0.27 × 0.11 × 0.05	0.11 × 0.06 × 0.03
index ranges	$-23 \le h \le 24$, $-5 \le k \le 5$, $-16 \le l \le 15$	$-21 \le h \le 14$, $-4 \le k \le 4$, $-15 \le l \le 13$
scan type	ω scans	ω scans
scan width	1°	1°
reflections collected	2831	2581
exposure time	25 s/frame	52 s/frame
independent reflections	982 [R(int) = 0.0396]	852 [R(int) = 0.0234]
completeness	99.2% (up to θ = 26.3°)	99.2% (up to θ = 25.3°)
X-ray radiation	Mo Kα, λ = 0.71073 Å	Mo Kα, λ = 0.71073 Å
X-ray power	50 kV, 40 mA	50 kV, 40 mA
absorption coefficient	42.85 mm^{-1}	5.69 mm^{-1}
theta range	3.46° to 29.39°	3.43° to 28.36°
$F(000)$	1344	960
refined parameters	99	99
final $R1/wR2$ [$I > 2\sigma(I)$]	0.0296/0.0626	0.0213/0.0429
$R1/wR2$ (all data)	0.0334/0.0643	0.0286/0.0453
goodness-of-fit on F^2	1.247	1.001

120.19(1)°, space group $C2/m$. To the best of our knowledge, for $TiTa_2O_7$, no single-crystal X-ray diffraction or Rietveld analysis data have been reported so far.

Because of the congruent melting behavior, the high-temperature resistance and the expected high hardness (short metal−oxygen bond distances), as well as excellent optical properties and usually good chemical resistance of titanium and tantalum/niobium oxides,[10,11] we decided to investigate $TiTa_2O_7$ and $TiNb_2O_7$ in more detail. The results of the hardness and elastic modulus measurements of $TiTa_2O_7$ and $TiNb_2O_7$ samples by the use of almost nondestructive nanonindentation are presented. Spectroscopic ellipsometry enabled the determination of the index of refraction (n) and extinction coefficient (k) in the spectral range from 245 nm to 1000 nm for the titanium tantalum and titanium niobium oxides. To complement the crystal structure data, the results of the single-crystal X-ray diffraction experiments, as well as Rietveld refinements are reported. Furthermore, the calculated thermal expansion tensors of $TiTa_2O_7$ and $TiNb_2O_7$, as a function of temperature, are related to structural changes.

2. EXPERIMENTAL SECTION

2.1. Synthesis. Large single crystals (>1000 μm) of $TiTa_2O_7$ and $TiNb_2O_7$ were grown directly from the melt at 1973 and 1873 K, respectively. Stoichiometric amounts of the dried starting materials (Alfa Aesar; Nb_2O_5, 99.999%; Ta_2O_5, 99.993%; TiO_2, >99%) were homogenized in a planetary ball mill with ethanol. The pressed mixtures were placed on an iridium sheet and fired in a muffle furnace from 1273 K to 1973/1873 K with a heating ramp of 5 K/min. After a dwell time of 10 min, the melt was cooled to 1173 K with a ramp of 0.5 K/min and subsequently quenched in air. Various polycrystalline $TiTa_2O_7$ and $TiNb_2O_7$ samples were additionally prepared by solid-state reactions in a platinum crucible at temperatures in the range between 1598 K and 1773 K. The isostatically pressed (15 kN/30 s) tablets were fired at different dwell times (10, 15, 20, 45, and 86 h). All samples were slowly cooled to 1073 K at a rate of 1.6 K/min and finally to 298 K with 0.8 K/min. This procedure resulted in the formation of smaller single crystals with a length up to 600 μm. Larger crystals showed a platy habit with basal planes parallel to $(10\bar{1})$, as derived from a detailed morphological analysis based on the orientation matrix determined by single-crystal diffraction. Noteworthy, this pronounced anisotropic morphology was reflected in a strong preferred orientation of the polycrystalline samples when studied via powder X-ray diffraction. For a better understanding of the collected Raman spectra, mixed crystals with a composition of $TiTaNbO_7$ were prepared at 1773 K and a dwell time of 45 h, followed by slow cooling (1.6 K/min) to ambient conditions.

2.2. X-ray Diffraction. Single-crystal diffraction experiments were performed on an Oxford Diffraction Gemini R Ultra diffractometer equipped with a Ruby CCD detector using graphite-monochromatized Mo Kα radiation. Prismatic, colorless single crystals with good optical quality were selected for structural investigations and mounted on the tip of a glass fiber using fingernail hardener. Structure solutions by direct methods and least-squares-refinement calculations were carried out with the programs SIR-92[12] and SHELXL-97,[13] respectively, embedded in the WinGX software suite (v1.80).[14] An absorption correction based on indexed faces has been applied using the data collection and processing software CrysAlis^{Pro} (Agilent).[15] The starting values (atomic coordinates) for the structure analyses were taken from the single-crystal studies by Gasperin (ICSD Entry No. 48109).

Table 2. Atomic Coordinates, Site Occupancies, and Equivalent Isotropic Displacement Parameters for $TiNb_2O_7$

atom	Wyckoff site	occupancy	x	y	z	U_{eq}
Nb(1)	2a	0.909(5)	0	0	0	0.0210(3)
Ti(1)	2a	0.091(5)	0	0	0	0.0210(3)
Nb(2)	4i	0.798(3)	0.18528(2)	0	0.17993(4)	0.00998(17)
Ti(2)	4i	0.202(3)	0.18528(2)	0	0.17993(4)	0.00998(17)
Nb(3)	4i	0.643(3)	0.07842(2)	0	0.44156(4)	0.00408(17)
Ti(3)	4i	0.357(3)	0.07842(2)	0	0.44156(4)	0.00408(17)
Nb(4)	4i	0.727(3)	0.88938(2)	0	0.25857(3)	0.00593(17)
Ti(4)	4i	0.273(3)	0.88938(2)	0	0.25857(3)	0.00593(17)
Nb(5)	4i	0.376(3)	0.29286(3)	0	0.92521(5)	0.0055(2)
Ti(5)	4i	0.624(3)	0.29286(3)	0	0.92521(5)	0.0055(2)
O(1)	4i	1	0.17350(15)	0	0.5767(2)	0.0058(6)
O(2)	4i	1	0.37287(15)	0	0.7931(2)	0.0056(6)
O(3)	4i	1	0.59702(15)	0	0.9748(2)	0.0058(6)
O(4)	4i	1	0.79131(15)	0	0.1744(2)	0.0092(6)
O(5)	4i	1	0.24932(15)	0	0.0540(2)	0.0085(6)
O(6)	4i	1	0.70916(16)	0	0.7059(2)	0.0063(6)
O(7)	4i	1	0.89988(16)	0	0.9149(2)	0.0121(7)
O(8)	4i	1	0.02523(15)	0	0.6080(2)	0.0075(6)
O(9)	4i	1	0.87451(16)	0	0.6853(2)	0.0093(6)
O(10)	2b	1	0.5	0	0.5	0.0153(10)
O(11)	4i	1	0.04964(15)	0	0.8521(2)	0.0105(6)

Table 3. Selected Bond Lengths (up to 2.5 Å) for $TiNb_2O_7$

bond pair	bond length [Å]	bond pair	bond length [Å]	bond pair	bond length [Å]
Nb/Ti(1)−O10	1.900(3)	Nb/Ti(3)−O9	1.789(3)	Nb/Ti(5)−O5	1.776(3)
Nb/Ti(1)−O10	1.900(3)	Nb/Ti(3)−O8	1.872(3)	Nb/Ti(5)−O4	1.814(3)
Nb/Ti(1)−O7	1.956(3)	Nb/Ti(3)−O3	1.963(3)	Nb/Ti(5)−O1	1.992(3)
Nb/Ti(1)−O7	1.956(3)	Nb/Ti(3)−O3	1.963(3)	Nb/Ti(5)−O1	1.992(3)
Nb/Ti(1)−O11	2.036(3)	Nb/Ti(3)−O1	2.215(3)	Nb/Ti(5)−O3	2.185(3)
Nb/Ti(1)−O11	2.036(3)	Nb/Ti(3)−O8	2.268(3)	Nb/Ti(5)−O2	2.209(3)
Nb/Ti(2)−O7	1.795(3)	Nb/Ti(4)−O11	1.777(3)		
Nb/Ti(2)−O5	1.959(3)	Nb/Ti(4)−O4	1.920(3)		
Nb/Ti(2)−O6	1.965(3)	Nb/Ti(4)−O2	1.972(3)		
Nb/Ti(2)−O6	1.965(3)	Nb/Ti(4)−O2	1.972(3)		
Nb/Ti(2)−O9	2.000(3)	Nb/Ti(4)−O8	2.086(3)		
Nb/Ti(2)−O6	2.203(3)	Nb/Ti(4)−O1	2.340(3)		

However, because of the smaller β-angle, the coordinates were transformed to the $I2/m$ setting of space group No. 12 ($C2/m$). Details of the data collection and refinement parameters for $TiTa_2O_7$ and $TiNb_2O_7$ are given in Table 1. Final full matrix least-squares refinement cycles, including fractional coordinates as well as anisotropic displacement parameters for all atoms, converged in the case of $TiNb_2O_7$ to a residual of $R1 = 0.0213$ for 852 reflections and in the case of $TiTa_2O_7$ to $R1 = 0.0296$ for 982 reflections with $I > 2\sigma(I)$. Refined coordinates, site occupancy values, equivalent isotropic displacement parameters, as well as selected interatomic distances for $TiNb_2O_7$ and $TiTa_2O_7$, are given in Tables 2−5. Anisotropic displacement parameters and selected angles are accessible in the Supporting Information (Tables S1−S4). Figures showing structural details were prepared using the program VESTA 3.1.[16]

High-resolution powder X-ray diffraction data were recorded under ambient conditions on a Bruker Model AXS D8 Discover powder diffractometer in Bragg−Brentano θ−θ geometry using strictly monochromatic Cu Kα_1 radiation (λ = 1.5406 Å; 40 kV, 40 mA) and a one-dimensional LYNXEYE silicon strip detector. The monochromatization of the Cu radiation was accomplished by a primary beam Ge(111) monochromator. Data acquisitions were performed in the 2θ range between 3° and 135°, using a step width of 0.005° and a counting time of 2 s per step. A fixed divergence slit (0.3°) and a secondary Soller slit were used. The structural data were refined by the Rietveld method,[17] using the TOPAS 4.2[18] software. X-ray line profile-fitting was carried out by the fundamental parameters approach.[19]

To determine the thermal expansion of the titanium tantalum and titanium niobium oxides, *in situ* high-temperature studies in the range of 323−1323 K (ΔT = 50 K per measurement) were performed with a Siemens D5005 powder X-ray diffractometer equipped with an Anton Paar Model HTK1200 high-temperature heating stage. Data were collected in the 2θ range between 5° and 90° with a step size of 0.02° and an acquisition time of 6 s per step. In order to achieve thermal equilibrium inside the chamber, the polycrystalline samples were kept at the target temperature for 5 min before the next measurement was started. The determination of the thermal expansion tensor α_{ij} from the powder diffraction data of $TiTa_2O_7$ and $TiNb_2O_7$ was carried out with the TEV (v0.9.4) program.[20]

2.3. Raman Spectroscopy. Confocal Raman spectra of the samples in the range of 50−4000 cm^{-1} were recorded with a Horiba Jobin Yvon Labram-HR 800 Raman microspectrometer. The samples were excited using the 532 nm emission line of a frequency-doubled 100 mW Nd:YAG laser and the 633 nm emission line of a 17 mW He−Ne laser under an Olympus 100× objective lens (numerical aperture of 0.9). The size of the laser spot on the surface was ~1 μm in diameter. The scattered light was dispersed by an optical grating with 1800 lines mm^{-1} and collected by a 1024 × 256 open-electrode CCD detector. The spectral resolution, determined by measuring the Rayleigh line, was <2 cm^{-1}. The spectra were recorded unpolarized

Table 4. Atomic Coordinates, Site Occupancies, and Equivalent Isotropic Displacement Parameters for $TiTa_2O_7$

atom	Wyckoff site	occupancy	x	y	z	U_{eq}
Ta(1)	2a	0.994(3)	0	0	0	0.0086(2)
Ti(1)	2a	0.006(3)	0	0	0	0.0086(2)
Ta(2)	4i	0.860(2)	0.18508(2)	0	0.18151(4)	0.00794(17)
Ti(2)	4i	0.140(2)	0.18508(2)	0	0.18151(4)	0.00794(17)
Ta(3)	4i	0.615(2)	0.07848(3)	0	0.44410(4)	0.0063(2)
Ti(3)	4i	0.385(2)	0.07848(3)	0	0.44410(4)	0.0063(2)
Ta(4)	4i	0.809(2)	0.88803(2)	0	0.25952(4)	0.00696(17)
Ti(4)	4i	0.191(2)	0.88803(2)	0	0.25952(4)	0.00696(17)
Ta(5)	4i	0.218(2)	0.29323(5)	0	0.92613(8)	0.0062(3)
Ti(5)	4i	0.782(2)	0.29323(5)	0	0.92613(8)	0.0062(3)
O(1)	4i	1	0.1732(3)	0	0.5764(6)	0.0060(13)
O(2)	4i	1	0.3722(3)	0	0.7933(5)	0.0065(13)
O(3)	4i	1	0.5969(3)	0	0.9734(5)	0.0072(13)
O(4)	4i	1	0.7914(3)	0	0.1734(5)	0.0088(14)
O(5)	4i	1	0.2504(4)	0	0.0557(6)	0.0115(14)
O(6)	4i	1	0.7100(4)	0	0.7064(6)	0.0071(13)
O(7)	4i	1	0.8996(3)	0	0.9162(5)	0.0105(15)
O(8)	4i	1	0.0253(3)	0	0.6083(6)	0.0086(14)
O(9)	4i	1	0.8748(4)	0	0.6857(6)	0.0127(15)
O(10)	2b	1	0.5	0	0.5	0.0183(24)
O(11)	4i	1	0.0489(4)	0	0.8519(6)	0.0128(16)

Table 5. Selected Bond Lengths (up to 2.5 Å) for $TiTa_2O_7$

bond pair	bond length [Å]	bond pair	bond length [Å]	bond pair	bond length [Å]
Ta/Ti(1)−O10	1.9006(2)	Ta/Ti(3)−O9	1.807(6)	Ta/Ti(5)−O5	1.769(6)
Ta/Ti(1)−O10	1.9006(2)	Ta/Ti(3)−O8	1.882(6)	Ta/Ti(5)−O4	1.819(7)
Ta/Ti(1)−O7	1.953(6)	Ta/Ti(3)−O3	1.954(2)	Ta/Ti(5)−O1	1.992(2)
Ta/Ti(1)−O7	1.953(6)	Ta/Ti(3)−O3	1.954(2)	Ta/Ti(5)−O1	1.992(2)
Ta/Ti(1)−O11	2.022(6)	Ta/Ti(3)−O1	2.186(6)	Ta/Ti(5)−O3	2.183(7)
Ta/Ti(1)−O11	2.022(6)	Ta/Ti(3)−O8	2.232(6)	Ta/Ti(5)−O2	2.192(5)
Ta/Ti(2)−O7	1.806(6)	Ta/Ti(4)−O11	1.800(6)		
Ta/Ti(2)−O5	1.963(6)	Ta/Ti(4)−O4	1.907(7)		
Ta/Ti(2)−O6	1.967(2)	Ta/Ti(4)−O2	1.967(1)		
Ta/Ti(2)−O6	1.967(2)	Ta/Ti(4)−O2	1.967(1)		
Ta/Ti(2)−O9	1.970(6)	Ta/Ti(4)−O8	2.088(7)		
Ta/Ti(2)−O6	2.179(7)	Ta/Ti(4)−O1	2.305(6)		

under ambient conditions. The accuracy of the Raman line shifts, calibrated by measuring a silicon standard, was on the order of 0.5 cm^{-1}. First- and second-order polynomial and convoluted Gaussian−Lorentzian functions were fitted to background and Raman bands, respectively, using the built-in spectrometer software LabSpec 5.[21] The calculation of the number and symmetry of the vibrational modes were carried out using the crystallographic information file and the SAM program.[22−25]

2.4. Electron Microprobe Analysis (EMPA) and Scanning Electron Microscopy (SEM). To perform electron microprobe analyses, $TiTa_2O_7$ and $TiNb_2O_7$ single crystals, as well as sintered polycrystalline tablets, were embedded in resin and polished to a mirror-like surface finish using diamond spray (Bigott, Germany). To ensure electric conductivity, the samples were coated with a thin carbon film. The measurements were performed using a JEOL Model JXA-8100 electron probe microanalyzer that was equipped for wavelength-dispersive X-ray spectrometry (WDS) and energy-dispersive X-ray spectrometry (EDS). Rutile, $Nb_2O_{4.98}$, and $Ta_2O_{4.93}$ standard crystals were used as references to ensure precise chemical analyses of titanium, niobium, and tantalum concentrations in the specimen. An acceleration voltage of 15 kV, a probe current of 10 nA, and an image magnification up to 30 000× were used. Backscattered electron (BSE) microscopy and secondary electron (SE) microscopy was used to image possible chemical differences, as well as the surface topography, respectively.

Using a high-resolution electron microscopy system (JEOL, Model JSM-6010 LV), analytical electron microscope images of the uncoated sample surfaces were obtained. SEM analysis provided a magnification range from 5× to 300 000× with a maximum resolution of 4 nm (SE image) and a simple change between high vacuum and low vacuum operation mode. Backscattered electron shadow (BES) images were acquired at low vacuum with an acceleration voltage of 15 kV.

2.5. Nanoindentation and Atomic Force Microscopy (AFM). Nanoindentation experiments were performed with a NanoTest Vantage instrument (Micro Materials, United Kingdom), which was equipped with a Berkovich diamond indenter tip to determine the mechanical properties of $TiTa_2O_7$ and $TiNb_2O_7$. The obtained load−displacement curves were analyzed by the built-in software using a power law fit (80% of maximum load, frame compliance = 0.428 nm/mN, $\varepsilon = 0.75$) and a diamond area function (with a Berkovich factor of $\beta = 1.034$). Post-indentation data were used for the thermal drift correction. In addition, the indents and surfaces of the samples were studied by AFM. For the contact mode measurements, a Nanosurf Nanite AFM system (Nanosurf AG, Switzerland) was used, which was equipped with an aluminum reflex coated cantilever and a rotated monolithic silicon probe (BudgetSensors, Innovative Solutions Bulgaria, Ltd.). In the static force operating mode, the force between the tip and the surface (18 nN) was kept constant and the deflection of the cantilever was used as the feedback signal.

2.6. Spectroscopic Ellipsometry. Optical constants of the polished Ta_2TiO_7 and Nb_2TiO_7 ceramics were determined with an M-2000U variable-angle ellipsometer (J. A. Woollam Co., Inc., USA). The system covers a spectral range from 245 nm to 1000 nm (470 wavelengths). All wavelengths could be detected simultaneously with a charge-coupled device (CCD). The amplitude component ψ and the change in phase difference Δ were measured at different angles of incidence (65°, 70°, 75°). Using the spectrometer software CompleteEase,[26] the index of refraction (n) and the extinction coefficient (k) could be calculated from the measured ψ/Δ values, as a function of wavelength. Assuming a homogeneous bulk, and because of the low surface roughness, the "pseudo" optical constants ($\langle n \rangle$ and $\langle k \rangle$) were directly transformed from the measured SE data.

3. RESULTS AND DISCUSSION

3.1. X-ray Diffraction and Electron Microscopy. Single-crystal X-ray diffraction experiments revealed that $TiTa_2O_7$ and $TiNb_2O_7$ are isostructural and consist of distorted $(Ti,Ta)O_6$/$(Ti,Nb)O_6$ octahedra, sharing corners and edges (Figure 1). Ti^{4+} and Nb^{5+}/Ta^{5+} have very similar ionic radii, in the case of 6-fold oxygen coordination (Ti^{4+}: 0.61 Å, Nb^{5+}/Ta^{5+}: 0.64 Å)[27] and, therefore, can easily substitute each other in octahedral coordination environments. Within the structure of $TiTa_2O_7$ and $TiNb_2O_7$, five crystallographically different octahedral sites (M1−M5) can be distinguished. The distortion of the octahedra can be expressed numerically by means of the quadratic elongation λ and the bond angle variance σ^2.[28] For $TiNb_2O_7$, these parameters have the following values (respectively): 1.002 and 0.04 (for M1), 1.027 and 80.08 (for M2), 1.051 and 145.78 (for M3), 1.045 and 126.75 (for M4), and 1.046 and 135.34 (for M5). In the case of $TiTa_2O_7$, the distortion parameters λ and σ^2 of the chemically different octahedra have the following values (respectively): 1.001 and 0.02 (for M1), 1.027 and 83.16 (for M2), 1.044 and 127.42 (for M3), 1.041 and 116.93 (for M4), and 1.046 and 133.91 (for M5). Thus, the octahedra of the M1 site, which are connected only by corners with neighboring polyhedra exhibit the lowest degree of distortion, while the edge- and corner-sharing octahedra around the M3 and M5 sites show the highest degree of distortion. The M2 octahedra are connected by edges (×2) only among themselves and by corners with other polyhedra (M1, M2, M3, M5). The M3 octahedra share four edges with M3, M4, and M5 (×2) and corners with M2, M3, and M4. In turn, the octahedra of the M4 site are connected via edges with three other polyhedra (M3, M5(×2)) and via corners with M1, M3, M4, M5. The distorted octahedra of the M5 site share four edges with two chemically different polyhedra (M3 (×2), M4 (×2)) and corners with M2, M4, and M5. Therefore, the degree of the polyhedral distortion relates to the number of shared edges. However, the average metal−oxygen bond distance of each individual octahedron is very similar. In the case of $TiTa_2O_7$, the M−O bond distances vary from 1.77 Å to 2.305 Å, with an average value of 1.99 Å, whereas the corresponding distances in $TiNb_2O_7$ are scattered between 1.78 Å and 2.34 Å, with an average bond distance of 2.00 Å.

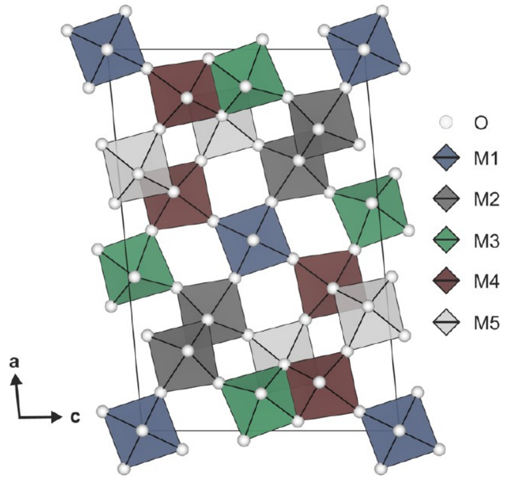

Figure 1. Crystal structure of $TiTa_2O_7$ in a projection parallel to [010]. Within the structure, five chemically different octahedral sites (M1− M5) can be distinguished.

The structure of both compounds exhibits fragments of the rhenium trioxide ReO_3 structure in the form of blocks, each containing nine corner-sharing MO_6 octahedra (Figure 2). These blocks are connected by edges along the [001] direction, or in more detail, between the M3 and M4 octahedra and built infinite columns along the [010] direction. In many transition metal oxides, crystallographic shear can be observed, where the reduction of the oxides (e.g., TiO_2, Nb_2O_5) results in the formation of crystallographic shear planes in preference to the creation of oxygen vacancies.[29] In the case of $TiTa_2O_7$ and $TiNb_2O_7$, the $(3 \times 3)_\infty$ blocks are bounded by crystallographic shear planes along [101] and [001]. Figure 3 displays the formation of endless linear columns (corner-sharing octahedra) and of zigzag chains (edge-sharing octahedra) along the crystallographic b-axis.

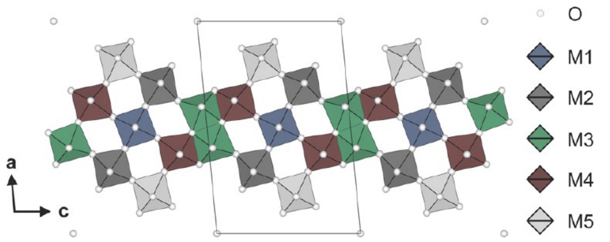

Figure 2. A 3.8-Å-wide slice of the structure at $y \approx 0.5$ exhibits fragments of the ReO_3 structure in the form of blocks. These blocks are constructed of nine corner-sharing octahedra and are connected by edges along the [001] direction. Small spheres represent O atoms.

Single-crystal structure refinements of $TiNb_2O_7$ and $TiTa_2O_7$ clearly confirmed a cation ordering among the crystallographically different metal sites (M1−M5). In both materials, the M1 site is almost fully occupied (>90%) by niobium or

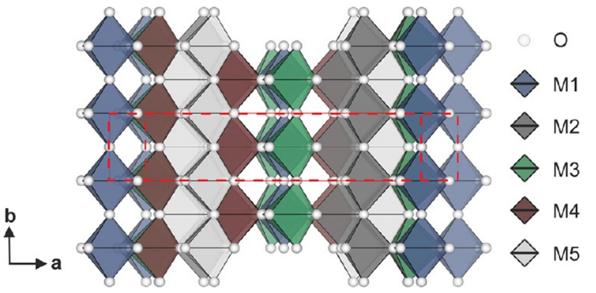

Figure 3. Octahedra joined by corners and edges built endless linear and zigzag chains, respectively, along the [010] direction. Red dashed lines display the unit cell; small spheres represent O atoms.

tantalum, respectively (see Figure 4). On the other hand, the M5 site is enriched in titanium (>60%). The metal sites M2 and M4 show occupancies with niobium or tantalum concentrations varying from 72.7% (Nb4) to 79.8% (Nb2), in the case of $TiNb_2O_7$, and from 80.9% (Ta4) to 86.0% (Ta2) in the case of $TiTa_2O_7$. However, the M3 cation site exhibits lower niobium (64.3%) and tantalum (61.5%) concentrations. According to Von Dreele and Cheetham,[8] the cation ordering can be explained by consideration of local charge balance or by electrostatic potential calculations. In our case, the M1 site requires a highly charged cation, because the polyhedra share only corners. Edge-sharing MO_6 octahedra, in turn, prefer lower charged cations. In $TiNb_2O_7$, the M1 site exhibits an average site charge of +4.91, the M5 site has an average site charge of +4.38, and, for the M2−M4 octahedral sites, the values range from +4.64 to +4.80. These values are in good agreement when compared with the published data in the work of Von Dreele and Cheetham.[8] In $TiTa_2O_7$, the charge distributions are slightly different. The M1 site shows a higher average site charge of +4.99 and a lower charge of +4.22 for the M5 site. The charge distribution for the M2−M4 octahedral sites vary from +4.62 to +4.86.

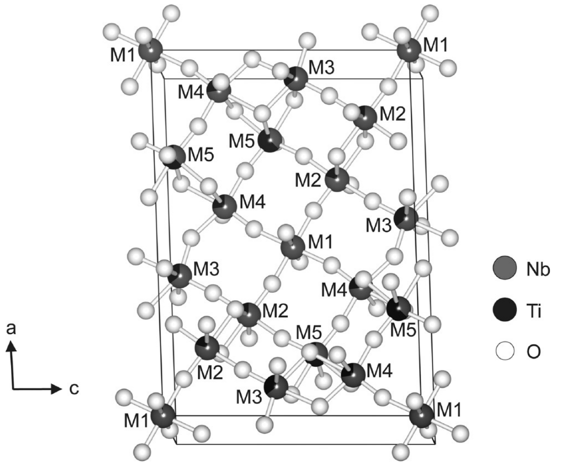

Figure 4. Projection of the unit cell (y_{min} = 0.5, y_{max} = 1) for $TiNb_2O_7$ parallel to [010]. Small spheres (white) represent O atoms. The five different octahedral sites (M1−M5) are occupied by Nb atoms (gray) and Ti atoms (black).

To complement the structural data of $TiTa_2O_7$ and $TiNb_2O_7$, Rietveld refinements have been performed from the powder diffraction data of the polycrystalline samples (see Figures S1 and S2 in the Supporting Information). The diffraction patterns of the $TiTa_2O_7$ and $TiNb_2O_7$ samples, which were fired at high temperatures (>1600 K) for more than 20 h, showed a strong preferred orientation along the $(10\bar{1})$. To reduce this preferred orientation, the polycrystalline samples were synthesized at 1598 K for a short time (2 × 10 h), including an intermediate grinding. This enabled better quality Rietveld refinements of the powder diffraction data of $TiTa_2O_7$ and $TiNb_2O_7$. The backscattered electron shadow (BES) images of three different $TiTa_2O_7$ tablets (Figure 5) clearly show a correlation of the sintering time and the size/habitus of the crystals. WDS analyses revealed that all samples are chemically homogeneous with Nb_2O_5:TiO_2 and Ta_2O_5:TiO_2 molar ratios of 1:1 (see Table S5 in the Supporting Information). The structure refinement of $TiTa_2O_7$ and $TiNb_2O_7$ converged at R_{wp} = 6.52, R_p = 4.88, χ^2 = 2.31 (R_{exp} = 4.30) and R_{wp} = 6.31, R_p = 4.60, χ^2 = 3.42 (R_{exp} = 3.41), respectively.

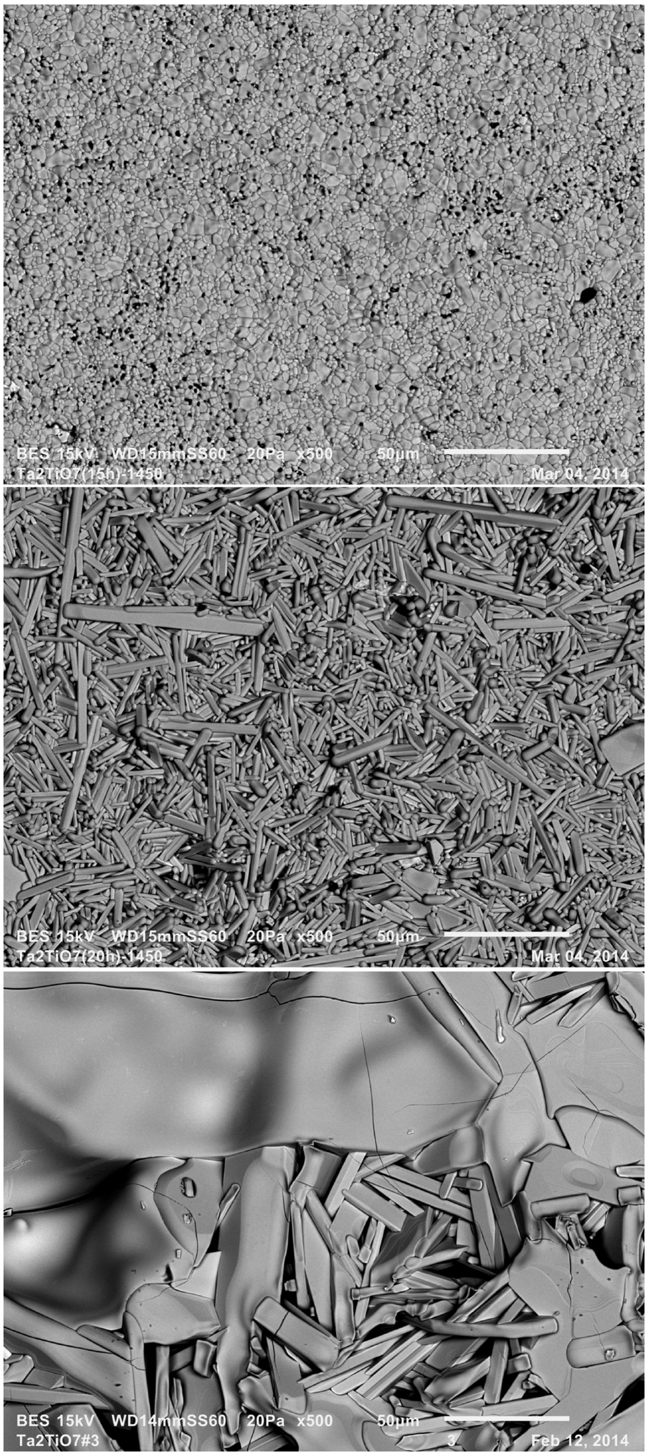

Figure 5. BES images of three unpolished Ta_2TiO_7 tablets fired at 1723 K for 15 h (top), 20 h (middle), and at 1773 K for 86 h (bottom). [Scale bar = 50 μm.] All samples were cooled from the target temperature to ambient conditions at a rate of 100 K/h.

3.2. Analysis of the Thermal Expansion.

In situ high-temperature powder X-ray diffraction experiments enabled the study of the thermal expansion of $TiTa_2O_7$ and $TiNb_2O_7$. Patterns were recorded from 323 K to 1323 K, in steps of 50 K. Whole powder pattern fitting of the diffractograms based on the LeBail method[30] was applied to determine the lattice parameters (see Table S6 in the Supporting Information). The refined values of the lattice parameters of $TiTa_2O_7$ are a = 17.68622(32) Å, b = 3.80626(06) Å, c = 11.85286(20) Å, β = 95.094(01)°, and V = 794.763(23) $Å^3$ at 323 K, and a = 17.73588(35) Å, b = 3.80577(07) Å, c = 11.90412(27) Å, β = 95.105(02)°, and V = 800.325(28) $Å^3$ at 1323 K. In the case of $TiNb_2O_7$, the values of the unit cell are a = 17.68831(32) Å, b = 3.80208(07) Å, c = 11.89533(23) Å, β = 95.324(02)°, and V = 796.538(25) $Å^3$ at 323 K, and a = 17.75082(51) Å, b = 3.79844(10) Å, c = 11.97253(29) Å, β = 95.305(02)°, and V = 803.795(38) $Å^3$ at 1323 K. These data indicate that only the values of the crystallographic a- and c-axes show significant variation, depending on the temperature (see Figures 6 and 7), while the values of the lattice parameters b and β are almost constant with the exception of minimal fluctuations. To calculate the components α_{ij} of the thermal expansion tensor the temperature dependence of the lattice parameters P over the temperature range of 323−1323 K have been fitted with second-order polynomials:

$$P(T) = p_0 + p_1 T + p_2 T^2 \tag{1}$$

where T is the temperature (given in Kelvin).

The quality of the fitting can be described numerically by the coefficient of determination R^2:

$$R^2 = \frac{\sum_{i=1}^{n} (a_i - \bar{a})^2 - \sum_{i=1}^{n} (a_i - \hat{a}_i)^2}{\sum_{i=1}^{n} (a_i - \bar{a})^2} \tag{2}$$

where a_i is the observed value for component i, $\hat{a}$ the calculated value for component i, $\bar{a}_i$ the mean, and n the number of different temperatures.[20]

The thermal expansion of a monoclinic crystal can be expressed by a second rank tensor of the form

$$\begin{bmatrix} \alpha_{11} & 0 & \alpha_{13} \\ 0 & \alpha_{22} & 0 \\ \alpha_{31} & 0 & \alpha_{33} \end{bmatrix} \tag{3}$$

where $\alpha_{13} = \alpha_{31}$. This tensor refers to an orthogonalized coordinate system $\{\mathbf{e}_1, \mathbf{e}_2, \mathbf{e}_3\}$. Within the TEV program,[20] $\mathbf{e}_3$ is chosen parallel to the crystallographic basis vector $\mathbf{c}$, $\mathbf{e}_2$ is parallel to $\mathbf{b}^*$, and $\mathbf{e}_1 = \mathbf{e}_2 \times \mathbf{e}_3$. The determination of the components α_{ij} of the thermal expansion tensor in the infinitesimal temperature limit was first described by Paufler and Weber.[31] By using the TEV program,[20] the tensor components in the temperature range of 323−1323 K were calculated for $TiTa_2O_7$ and $TiNb_2O_7$ (see Table S7 in the Supporting Information) and the three-dimensional (3-D) representation surface for the second rank tensor at 323 K (Figure 8), as well as two-dimensional (2-D) sections at 323, 532, 773, 1023 and 1273 K were plotted for the titanium tantalum (Figure 9) and titanium niobium oxide (Figure 10). Both materials exhibit low tensor component values with a maximum of 4.0992 × 10^{-6} K^{-1} (α_{33}) at 1323 K for $TiTa_2O_7$ and 7.5621 × 10^{-6} K^{-1} (α_{33}) at 1323 K in the case of $TiNb_2O_7$. It is obvious from Figure 8 that, at 323 K, the largest thermal expansion occurs parallel to [001] and the lowest parallel to [010] and $TiNb_2O_7$ shows a slightly higher thermal expansion, compared to $TiTa_2O_7$. Along the crystallographic b-axis, even negative thermal expansion values can be partly observed. At higher temperatures, the thermal expansion parallel to the a-axis increases more than that parallel to the c-axis. By relating the thermal expansion data with the crystal structure of $TiTa_2O_7$ and $TiNb_2O_7$, it is visible that maximum thermal expansion occurs perpendicular to the endless linear columns and zigzag chains of the corner- and edge-sharing octahedra, respectively.

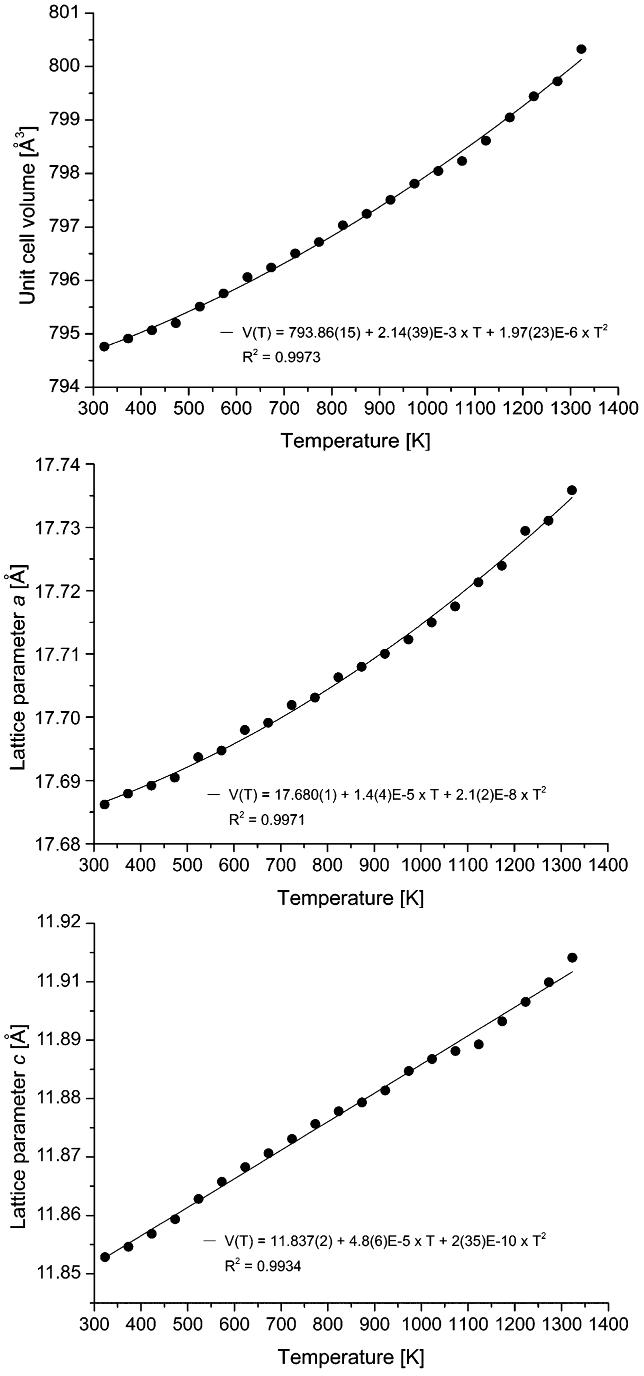

Figure 6. Evolution of the unit-cell volume and of the a- and c-lattice parameters for $TiTa_2O_7$.

3.3. Raman Spectroscopy.

From the selection rules of factor group C_{2h} (space group type $I2/m$), a total number of 114 vibrational modes are predicted for monoclinic $TiTa_2O_7$ and $TiNb_2O_7$ with the irreducible representations $\Gamma_{opt} = 36A_g + 20A_u + 18B_g + 40B_u$. These calculations for the monoclinic structure show that 54 modes ($36A_g + 18B_g$) are Raman-active, while 60 modes are IR-active ($20A_u + 40B_u$). In addition, $1A_u$ +

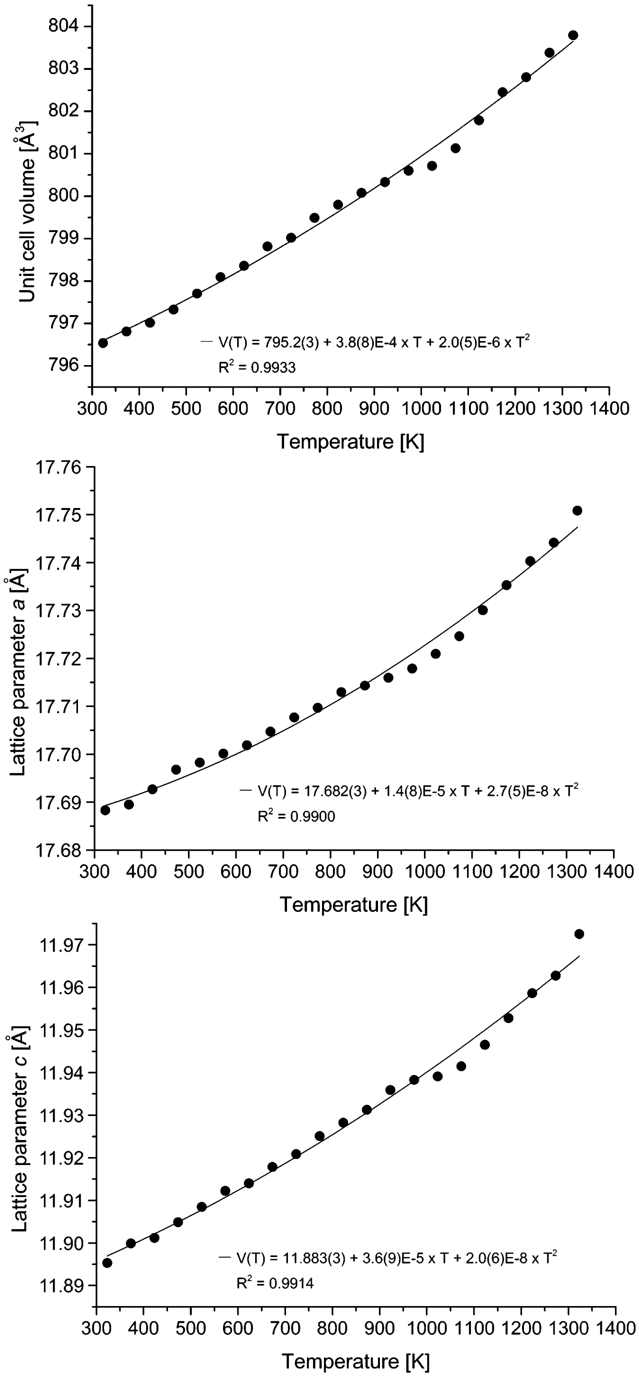

Figure 7. Evolution of the unit-cell volume and of the *a*- and *c*-lattice parameters for $TiNb_2O_7$.

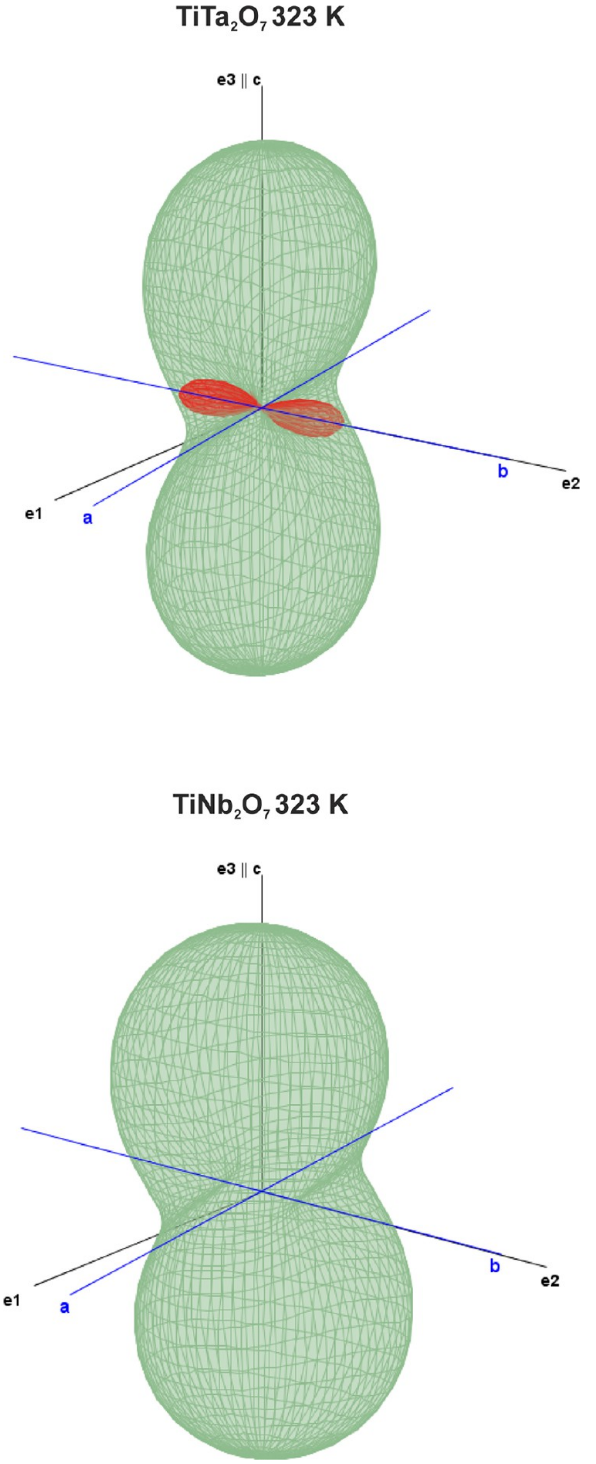

Figure 8. Three-dimensional (3-D) representation surface of the thermal expansion tensor for $TiTa_2O_7$ and $TiNb_2O_7$ at 323 K. In the case of $TiTa_2O_7$, red parts of the surface in the figure indicate directions with negative values of thermal expansion. $TiNb_2O_7$ shows a slightly higher thermal expansion, compared to $TiTa_2O_7$.

$2B_u$ modes are acoustic. As a result, only nondegenerated modes are expected in the Raman spectrum. Eror and Balachandran[32,33] previously studied polycrystalline $TiTa_2O_7$ and $TiNb_2O_7$ samples by vibrational spectroscopy but they estimated only a total number of 87 ($3N - 3$, $N = 30$) modes and observed 19 modes in the Raman spectrum of $TiTa_2O_7$ and 15 modes in the spectrum of $TiNb_2O_7$. In our investigation, it was possible to detect more than 25 Raman modes for both compounds by deconvolution of the Raman spectra (see Figures S3–S8 in the Supporting Information). A comparison of the Raman spectrum of $TiTa_2O_7$, $TiTaNbO_7$, and $TiNb_2O_7$, excited with the 532 nm emission line of a frequency-doubled Nd:YAG laser, is given in Figure 11. These measurements were conducted on the $(10\bar{1})$ plane of the crystals. The Raman spectrum of Ta_2TiO_7 exhibits strong Raman bands at 1020, 694, 673, 576, 298, 279, 260, 115, 95, and 75 cm^{-1}, medium modes at 898, 641, 382, 359, 223, 184, 128, 78, and 70 cm^{-1}, and weak bands at 1059, 832, 502, 318, 245, 206, and 143 cm^{-1}. The Raman spectrum of $TiNb_2O_7$ shows strong Raman bands

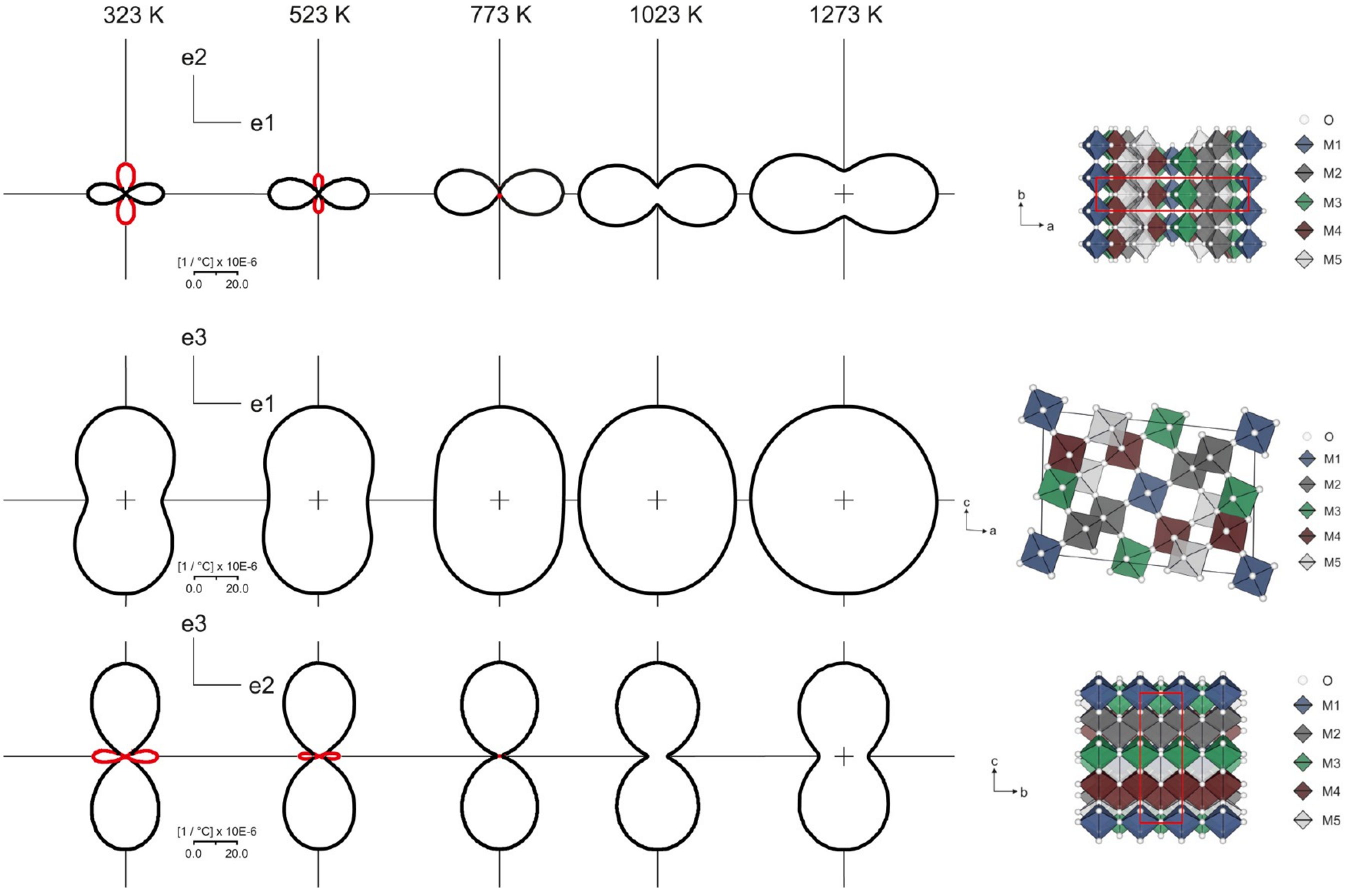

Figure 9. Sections through the 3-D representation surface for $TiTa_2O_7$ at 323, 523, 773, 1023, and 1273 K correlated with projections of the crystal structure.

at 1000, 650, 631, 538, 288, 270, 258, 133, 113, 85 cm^{-1}, medium modes at 887, 604, 373, 347, 221, 171, 97, 83 and weak bands at 1024, 838, 697, 473, 317, 232, and 202 cm^{-1}. In the case of single crystals, the intensity of the Raman bands is dependent on the orientation of the crystals, which could be especially observed in the high-wavenumber region (>850 cm^{-1}) of the Raman spectrum (Figure 12). The Raman spectra of $TiTa_2O_7$ and $TiTaNbO_7$ in Figure 11 clearly show that, above 150 cm^{-1}, the Raman modes are shifted to higher wavenumbers, compared to the vibrational modes of $TiNb_2O_7$; however, in the low-wavenumber region (<150 cm^{-1}), the Raman bands are shifted to lower frequencies. The most intense Raman mode of $TiNb_2O_7$ occurs at 113 cm^{-1} and that of $TiTa_2O_7$ occurs at 95 cm^{-1}. According to Eror and Balachandran,[32] the two bands at 899 and 1020 cm^{-1} in the Raman spectrum of $TiTa_2O_7$ can be assigned to the symmetric metal−oxygen stretching vibrations (ν_1) of the corner- and edge-shared TaO_6 octahedra, respectively, whereas metal−oxygen vibrations of the TiO_6 octahedra occur in the wavenumber region between 550 and 700 cm^{-1}. In our case, the ν_1 mode of the edge-shared TaO_6 octahedra can be observed at the same frequency (1020 cm^{-1}) and in the Raman spectra of $TiTaNbO_7$ and $TiNb_2O_7$ at 1010 and 1000 cm^{-1}, respectively, showing a linear correlation between the frequency of the mode and the niobium/tantalum concentration. Therefore, one could think about a semiquantitative chemical analysis of solid solutions ($TiTa_{2-x}Nb_xO_7$) by determining the position of the ν_1 stretching vibration. The shift of the Raman bands to higher frequencies can be explained by the higher bond strength and force constants of Ta−O bonds compared to Nb−O bonds. This trend correlates with the structural data, which show slightly shorter Ta−O and Ti−O bond distances ranging from 1.77 Å to 2.31 Å. The M−O bond distances of the $(Nb,Ti)O_6$ octahedra vary from 1.78 Å to 2.34 Å. This trend reveals that predominantly vibrations of the O atoms lead to vibrational modes >150 cm^{-1}, while the metal atoms located in the center of the atoms of the octahedra are not moving. According to Nakamoto,[34] within the same family of the periodic table, the stretching frequencies decrease as the mass of the central atom of the octahedra increase. This correlation can explain the shift of the Raman bands to lower frequencies in the low-wavenumber region (<150 cm^{-1}) and, therefore, the intense Raman modes can be related to vibrations of the metal atoms. M1-site cations, as well as O(10) atoms, generate no Raman-active vibrations, because of the symmetry restrictions (Wyckoff position 2a, 2b). Raman modes between 150 and 400 cm^{-1} can be probably assigned to O−Ti−O, O−Nb−O, or O−Ta−O symmetric and antisymmetric bending vibrations. Nakamoto[34] also pointed out that the higher the oxidation state, the higher the frequency. Therefore, Ti−O vibrations should be visible at lower frequencies than Ta−O or Nb−O vibrations, but only if the metal atoms participate in the vibration. In consequence of the strong variation of the metal−oxygen bond distances, the Raman modes of the M−O stretching vibrations are expected to occur in a wide wavenumber range.

3.4. Nanoindentation. This method allows the determination of mechanical properties of materials directly from

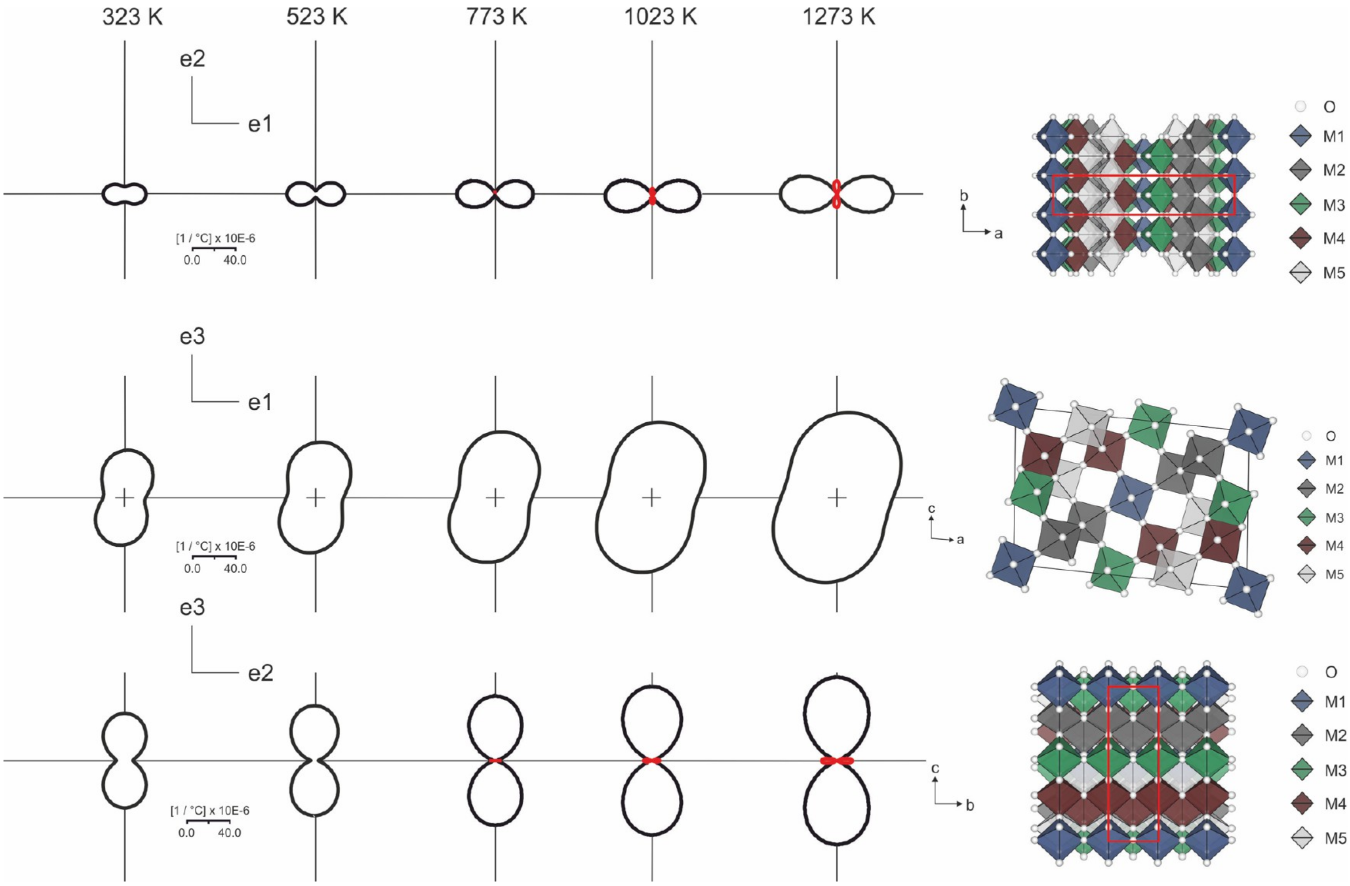

Figure 10. Sections through the 3-D representation surface for $TiNb_2O_7$ at 323, 523, 773, 1023, and 1273 K correlated with projections of the crystal structure.

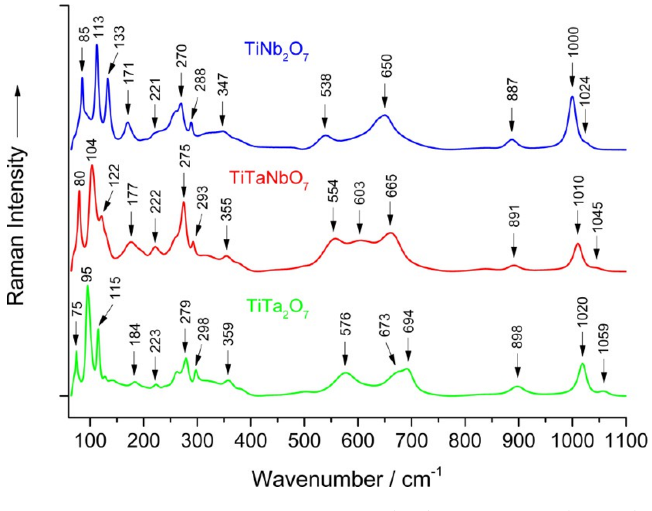

Figure 11. Raman spectra of $TiNb_2O_7$ (top), $TiTaNbO_7$ (middle), and $TiTa_2O_7$ (bottom) in the region between 60 and 1100 cm^{-1}, excited with the 532-nm emission line.

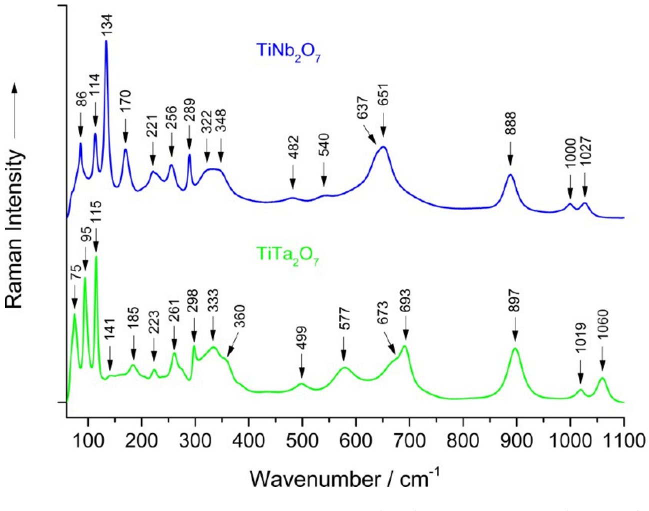

Figure 12. Raman spectra of $TiNb_2O_7$ (top) and $TiTa_2O_7$ (bottom) single crystals in the region between 60 cm^{-1} and 1100 cm^{-1}. The M–O stretching vibrations at 1000 ($TiNb_2O_7$) and 1019 cm^{-1} ($TiTa_2O_7$), respectively, show much lower intensities, compared to the Raman spectra in Figure 11.

indentation load and displacement measurements without the need to image the residual impression, as in the case of conventional indentation tests.[35] This enables the investigation of properties at the micrometer and nanometer scale and can therefore, for example, be used to analyze thin films as well as small crystals. Measurement of hardness and elastic modulus by instrumented indentation techniques was introduced by Oliver and Pharr.[36,37] All materials undergo elastic recovery when load is removed from the indenter. This elastic recovery leads to the unloading load–displacement curve and forms the basis of the analysis techniques that are used to calculate modulus and hardness of the specimen. For the analysis of the mechanical properties, four parameters must be defined from the load–displacement data: the maximum load (P_{max}), the maximum displacement (h_{max}), the elastic unloading stiffness ($S = dP/dh$, which defines the slope of the upper portion of the unloading curve), and the final depth (h_f) of the indent. With these parameters and the known geometry of the intender, an indirect determination of the contact area is possible and thus the hardness and elastic modulus of the material can be calculated.

According to Oliver and Pharr, the hardness H can be calculated from the equation

$$H = \frac{P_{max}}{A} \tag{4}$$

where A represents the contact area and P_{max} is the maximum load.

By measuring the unloading stiffness S, the reduced elastic modulus E_r can be defined from the relation

$$S = \beta\left(\frac{2}{\sqrt{\pi}}\right)E_r\sqrt{A} \tag{5}$$

where β is the Berkovich factor ($\beta = 1.034$).

With reference to this equations, analyses of the load−displacement curves (Figure 13) resulted in a hardness of H = 9.0 ± 0.5 GPa and a reduced elastic modulus of E_r = 170 ± 7 GPa for $TiTa_2O_7$. $TiNb_2O_7$ showed a slightly lower hardness of H = 8.7 ± 0.3 GPa and a reduced elastic modulus of E_r = 159 ± 4 GPa. The Young's modulus (E) is related to E_r by the following equation:

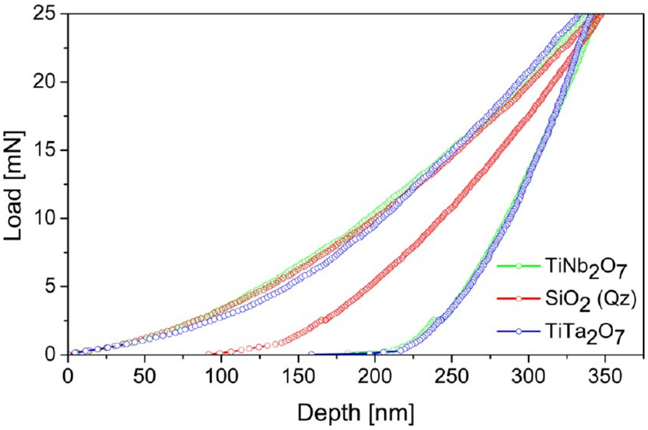

Figure 13. Load−displacement curves of $TiNb_2O_7$, $TiTa_2O_7$, and quartz (reference material).

$$\frac{1}{E_r} = \frac{1-\nu^2}{E} + \frac{1-\nu_i^2}{E_i} \tag{6}$$

where ν is the Poissońs ratio of the sample, E_i and ν_i are the parameters of the diamond indenter. The reduced elastic modulus (E_r) of the sample is obtained from the analysis of the load−displacement curves. For the calculation of the Young's modulus of $TiTa_2O_7$ and $TiNb_2O_7$, a Young's modulus of 1141 GPa (E_i) and a Poisson's ratio of 0.07 (ν_i) were used for the diamond indenter and a Poisson's ratio of 0.25 was used for the samples. With this data, a Young's modulus of E = 187 ± 9 GPa was calculated for $TiTa_2O_7$, and E = 173 ± 5 GPa, in the case of $TiNb_2O_7$.

The measured hardness H can also be converted to the widely used Vickers hardness H_V by the equation[35]

$$H_V = 94.495H \tag{7}$$

This results in a Vickers hardness (number) of H_V = 850 ± 47 for $TiTa_2O_7$ and H_V = 822 ± 28 for $TiNb_2O_7$.

In the case of synthetic quartz (reference material), analysis of the load−displacement curves revealed a hardness of H = 11.8 ± 0.4 GPa and a reduced elastic modulus of E_r = 98 ± 0.8 GPa. These data correspond to a Vickers hardness (number) of H_V = 1115 ± 38 and a Young's modulus of 106 ± 1 GPa. For the calculations of the Young's modulus of quartz, a Poisson's ratio of 0.10 was used.[38] The experimentally determined elastic modulus and hardness of the quartz sample are in good agreement with previous literature data.[39−43]

AFM analysis (Figure 14) show indents with a maximum depth of 300 ± 7 nm (at 20 mN). No formation of cracks or piling-up around the indents could be observed (Figure 15).

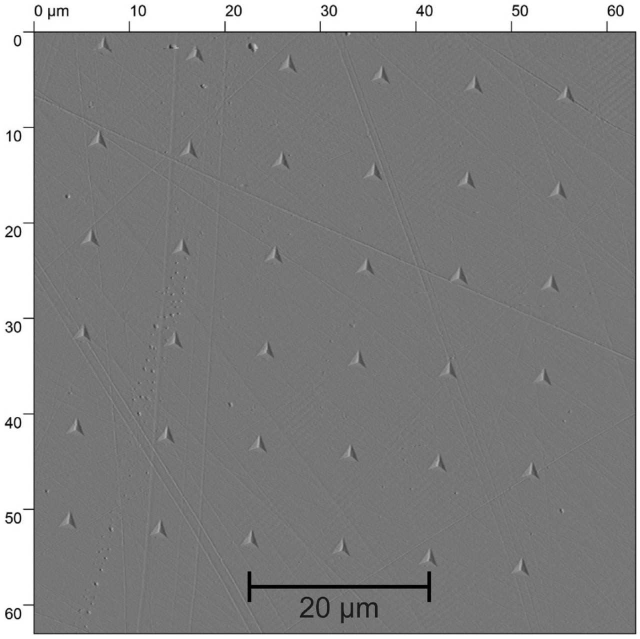

Figure 14. AFM micrograph of the residual impressions (10 μm distance).

3.5. Spectroscopic Ellipsometry.

Spectroscopic ellipsometry enabled the determination of the refractive index ⟨n⟩ (see Figures 16 and 17) and the extinction coefficient ⟨k⟩ (see

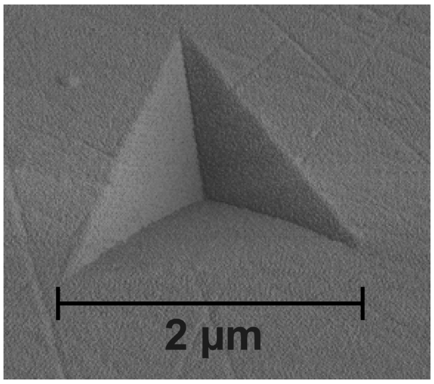

Figure 15. 3-D AFM micrograph of a residual impression. No formation of cracks or piling-up could be observed around the indents.

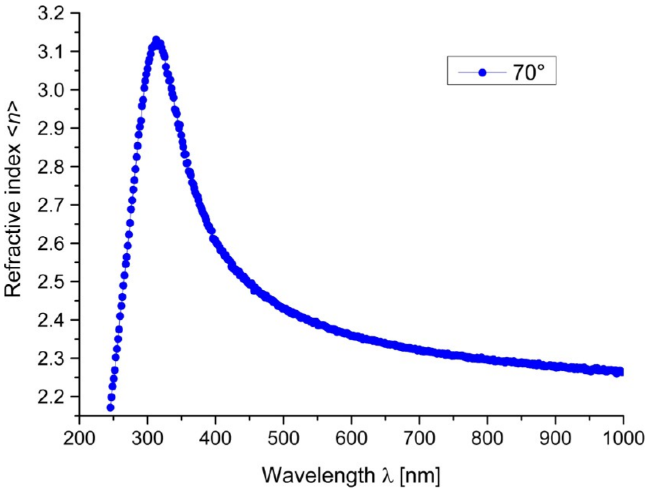

Figure 16. Refractive index ⟨n⟩, as a function of the wavelength, for a $TiNb_2O_7$ ceramic. The SE data were measured at an angle of incidence of 70°.

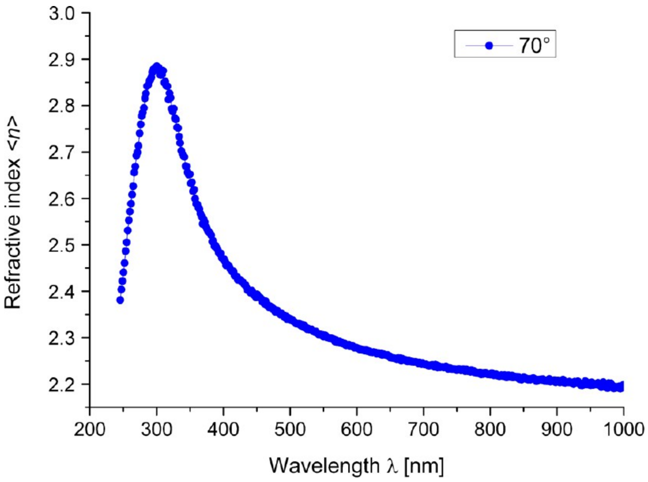

Figure 17. Refractive index ⟨n⟩, as a function of the wavelength, for a $TiTa_2O_7$ ceramic. The SE data were measured at an angle of incidence of 70°.

Figures S9 and S10 in the Supporting Information) of the polished $TiNb_2O_7$ and $TiTa_2O_7$ bulk ceramic samples. Three different spots on the surface were measured for each specimen, and the mean values were calculated. As we could see from the AFM images, the polished samples exhibited a very low surface roughness. $TiNb_2O_7$ shows a dispersion of 0.2, which is due to the variation of the refractive index from 2.53 ± 0.01 (at 430.79 nm, Fraunhofer G-line) and 2.33 ± 0.01 (686.72 nm, Fraunhofer B-line). The maximum index of refraction is 3.12 ± 0.02 at 318 nm. On the other hand, $TiTa_2O_7$ shows a dispersion of 0.17, because of the variation of the refractive index from 2.42 ± 0.01 (at 430.79 nm, Fraunhofer G-line) and 2.25 ± 0.01 (686.72 nm, Fraunhofer B-line). The maximum index of refraction is 2.88 ± 0.02 at 300 nm. The extinction coefficient k of $TiNb_2O_7$ and $TiTa_2O_7$ decreases from 0.5 to 0.0 in the wavelength range of 325–1000 and 308–1000 nm, respectively. In the visible spectrum, a normal dispersion behavior can be observed, i.e., the decrease of the refractive index with increasing wavelength. However, below 318 nm ($TiNb_2O_7$) and 300 nm ($TiTa_2O_7$), respectively, an anomalous dispersion behavior occurs, indicating an association of the absorption band with electronic oscillations.[44] $TiNb_2O_7$ exhibits a slightly higher refractive index, compared with $TiTa_2O_7$. Notably, $TiNb_2O_7$ ($\langle n\rangle_D = 2.37$) and $TiTa_2O_7$ ($\langle n\rangle_D = 2.29$) show a similar refractive index as that of diamond ($n = 2.417$ at $\lambda = 589$ nm).[45] Generally, refractive indices vary for light polarized along the three principal axes of the optical indicatrix of optically biaxial crystals. This results in different refractive indices of anisotropic crystals, depending on their orientation. In this work, we present the fundamental (average) optical properties of $TiTa_2O_7$ and $TiNb_2O_7$. For a precise experimental investigation of the optical anisotropy, in terms of determining the values of the three principal refractive indices n_α, n_β, and n_γ of $TiNb_2O_7$ and $TiTa_2O_7$, the growth of bigger single crystals (for example, using flame fusion) would be necessary.

In addition, for the purpose of comparison, the Gladstone–Dale relation[46] was used to calculate the mean refractive index of $TiNb_2O_7$ and $TiTa_2O_7$. Different mathematical approaches exist to obtain optical properties of materials, but the advantages of the Gladstone–Dale relation are the simplicity and generally excellent agreement with experimental investigations.[47] The relation can be expressed by the equation

$$K = \frac{n-1}{d} = \frac{k_1p_1}{100} + \frac{k_2p_2}{100} + \cdots \frac{k_np_n}{100} \tag{8}$$

where K is the specific refractive energy of a substance, d the density, k the specific refractive energies (Gladstone–Dale constants), and p the weight percentages of the components. Larsen[48] and Mandarino[49] determined the Gladstone–Dale constants k by investigating various chemical compounds. In our case, a mean refractive index of $\bar{n} = 2.34$ and $\bar{n} = 2.26$ could be calculated for $TiNb_2O_7$ and $TiTa_2O_7$, respectively, corresponding well with the experimental SE data.

4. CONCLUSIONS

In this contribution, the results of the thermal expansion analyses, as well as mechanical and optical properties, of $TiTa_2O_7$ and $TiNb_2O_7$ are reported. Furthermore, the structural data of the two chemical compounds were complemented by single-crystal X-ray diffraction experiments and Rietveld analyses, which clearly confirmed a cation ordering among the crystallographically different octahedral sites (M1–M5). Because of the high average refractive index, the relative high hardness, and the temperature behavior of $TiTa_2O_7$ and $TiNb_2O_7$, these materials could be of interest for further applications, e.g., optical coatings, synthetic gemstones, or low-thermal-expansion materials.

■ ASSOCIATED CONTENT

Ⓢ Supporting Information

Crystallographic information files (CIF), selected bond angles, and anisotropic displacement parameters, as well as Rietveld analyses data and coefficients of the thermal expansion tensors, are given for $TiTa_2O_7$ and $TiNb_2O_7$. In addition, deconvolution of the Raman spectra and the results of the wavelength-dispersive X-ray spectroscopy (WDS) analyses for $TiTa_2O_7$, $TiTaNbO_7$, and $TiNb_2O_7$ are presented. The Supporting Information is available free of charge on the ACS Publications website at DOI: 10.1021/acs.inorgchem.5b00733.

AUTHOR INFORMATION

Corresponding Author

*E-mail: Lukas.Perfler@uibk.ac.at.

Notes

The authors declare no competing financial interest.

ACKNOWLEDGMENTS

Financial support for this project has been obtained from the Austrian Research Promotion Agency (FFG): 829673, B2. Special thanks go to University Prof. Dr. Roman Lackner and Assistant Prof. Dr. Andreas Saxer for providing the nanoindenter, as well as Dr. Florian Pfuner for the ellipsometric measurements.

REFERENCES

(1) Shannon, R. D.; Shannon, R. C.; Medenbach, O.; Fischer, R. X. *J. Phys. Chem. Ref. Data* **2002**, *31*, 931−970.

(2) Yamanaka, S.; Kurosaki, K.; Maekawa, T.; Matsuda, T.; Kobayashi, S.; Uno, M. *J. Nucl. Mater.* **2005**, *344*, 61−66.

(3) Verdyan, A.; Soifer, Y. M.; Azoulay, J.; Rabkin, E.; Kazakevich, M. *IEEE Trans. Appl. Supercond.* **2005**, *15*, 3585−3588.

(4) Roth, R. S.; Coughanour, L. W. *J. Res. Natl. Bur. Stand.* **1955**, *55*, 209−213.

(5) Waring, J. L.; Roth, R. S. *J. Res. Natl. Bur. Stand.* **1968**, *72A*, 175−186.

(6) Jongejan, A.; Wilkins, A. L. *J. Less-Common Met.* **1969**, *19*, 185−191.

(7) Wadsley, A. D. *Acta Crystallogr.* **1961**, *14*, 660−664.

(8) Von Dreele, R. B.; Cheetham, A. K. *Proc. R. Soc. London A* **1974**, *338*, 311−326.

(9) Gasperin, M. *J. Solid State Chem.* **1984**, *53*, 144−147.

(10) Baboian, R. *Corrosion Tests and Standards: Application and Interpretation*, 2nd Edition; ASTM International: West Conshohocken, PA, 2005.

(11) Chu, A. K.; Chuang, M. J.; Hsieh, K. Y.; Huang, H. L.; Yu, Y. C.; Wang, C. W.; Lin, E. K. *J. Electron. Mater.* **1999**, *28*, 1457−1460.

(12) Altomare, A.; Cascarano, G.; Giacovazzo, C.; Guagliardi, A.; Burla, M. C.; Polidori, G.; Camalli, M. *J. Appl. Crystallogr.* **1994**, *27*, 435.

(13) Sheldrick, G. M. *Acta Crystallogr., Sect A: Found. Crystallogr.* **2008**, *A64*, 112−122.

(14) Farrugia, L. J. *J. Appl. Crystallogr.* **1999**, *32*, 837−838.

(15) *Agilent CrysAlis*^{PRO}; Agilent Technologies: Yarnton, U.K., 2012.

(16) Momma, K.; Izumi, F. *J. Appl. Crystallogr.* **2011**, *44*, 1272−1276.

(17) Rietveld, H. M. *J. Appl. Crystallogr.* **1969**, *2*, 65−71.

(18) *TOPAS Version 4.2: General Profile and Structure Analysis Software for Powder Diffraction Data*; Bruker AXS GmbH: Karlsruhe, Germany, 2009.

(19) Cheary, R. W.; Coelho, A. A. *J. Appl. Crystallogr.* **1992**, *25*, 109−121.

(20) Langreiter, T.; Kahlenberg, V. *Crystals* **2015**, *5*, 143−153.

(21) *S.A.S., LabSpec Version 5*; Horiba Jobin Yvon: Longjumeau Cedex, France, 2010.

(22) Aroyo, M. I.; Perez-Mato, J. M.; Orobengoa, D.; Tasci, E.; Flor, G.; Kirov, A. *Bulg. Chem. Commun.* **2011**, *43*, 183−197.

(23) Aroyo, M. I.; Perez-Mato, J. M.; Capillas, C.; Kroumova, E.; Ivantchev, S.; Madariaga, G.; Kirov, A.; Wondratschek, H. *Z. Kristallogr.* **2006**, *221*, 15−27.

(24) Aroyo, M. I.; Kirov, A.; Capillas, C.; Perez-Mato, J. M.; Wondratschek, H. *Acta Crystallogr., Sect. A: Found. Crystallogr.* **2006**, *A62*, 115−128.

(25) Kroumova, E.; Aroyo, M. I.; Perez-Mato, J. M.; Kirov, A.; Capillas, C.; Ivantchev, S.; Wondratschek, H. *Phase Transitions* **2003**, *76*, 155−170.

(26) *Complete EASE*; J.A. Woollam Co., Inc.: Lincoln, NE, USA, 2008.

(27) Shannon, R. D. *Acta Crystallogr., Sect. A: Cryst. Phys., Diffr., Theor. Gen. Crystallogr.* **1976**, *A32*, 751−767.

(28) Robinson, K.; Gibbs, G. V.; Ribbe, P. H. *Science* **1971**, *172*, 567−570.

(29) Andersson, S.; Wadsley, A. D. *Nature* **1966**, *211*, 581−583.

(30) Le Bail, A. *Powder Diffr.* **2005**, *20*, 316−326.

(31) Paufler, P.; Weber, Z. *Eur. J. Mineral.* **1999**, *11*, 721−730.

(32) Eror, N. G.; Balachandran, U. *Spectrochim. Acta* **1983**, *39*, 261−263.

(33) Eror, N. G.; Balachandran, U. *J. Solid State Chem.* **1982**, *45*, 276−279.

(34) Nakamoto, K. *Infrared and Raman Spectra of Inorganic and Coordination Compounds, Part A: Theory and Applications in Inorganic Chemistry*, 5th Edition; John Wiley & Sons, Inc.: New York, 1997.

(35) Fisher-Cripps, A. C. *Nanoindentation*, 3rd Edition; Mechanical Engineering Series 1; Springer: New York, 2011.

(36) Oliver, W. C.; Pharr, G. M. *J. Mater. Res.* **1992**, *7*, 1564−1583.

(37) Oliver, W. C.; Pharr, G. M. *J. Mater. Res.* **2004**, *19*, 3−20.

(38) Holm, B.; Rajeev, A. *J. Chem. Phys.* **1999**, *111*, 2071−2074.

(39) Mcskimin, H. J.; Anreatch, P.; Thurston, R. N. *J. Appl. Phys.* **1965**, *36*, 1624−1632.

(40) Taylor, E. W. *Mineral. Mag.* **1949**, *28*, 718−721.

(41) Goldsby, D. L.; Rar, A.; Pharr, G. M.; Tullis, T. E. *J. Mater. Res.* **2004**, *19*, 357−365.

(42) Evans, B. *J. Geophys. Res.* **1984**, *89*, 4213−4222.

(43) Scholz, C. H.; Engelder, J. T. *Int. J. Rock Mech. Min. Sci. Geomech. Abstr.* **1976**, *13*, 149−154.

(44) Chen, T.-C.; Desu, S. B. *Phys. Status Solidi A* **1998**, *167*, 215−221.

(45) Peter, F. *Z. Phys.* **1923**, *15*, 358−368.

(46) Gladstone, J. H.; Dale, T. P. *Philos. Trans. R. Soc. London* **1864**, *153*, 317−343.

(47) Mandarino, J. A. *Can. Mineral.* **2007**, *45*, 1307−1324.

(48) Larsen, E. S. *U.S. Geol. Surv. Bull.* **1921**, *679*, 1−294.

(49) Mandarino, J. A. *Can. Mineral.* **1976**, *153*, 498−502.

DOI: 10.1021/acs.inorgchem.5b00733
Inorg. Chem. 2015, 54, 6836−6848